

Large anomalous Hall effect in a hexagonal ferromagnetic Fe₅Sn₃ single crystal

Hang Li^{1,4}, Bingwen Zhang², Jinghua Liang³, Bei Ding^{1,4}, Jie Chen^{1,4}, Jianlei Shen^{1,4}, Zefang Li^{1,4}, Enke Liu^{1,5}, Xuekui Xi¹, Guangheng Wu¹, Yuan Yao¹, Hongxin Yang^{3,4} and Wenhong Wang^{1,5*}

¹Beijing National Laboratory for Condensed Matter Physics, Institute of Physics, Chinese Academy of Sciences, Beijing 100190, China

²Fujian Provincial Key Laboratory of Functional Marine Sensing Materials, Center for Advanced Marine Materials and Smart Sensors, Minjiang University, Fuzhou 350108, China

³Ningbo Institute of Materials Technology and Engineering, Chinese Academy of Sciences, Ningbo 315201, China

⁴University of Chinese Academy of Sciences, Beijing 100049, China

⁵Songshan Lake Materials Laboratory, Dongguan, Guangdong 523808, China

Abstract

In this paper, we report an experimental observation of the large anomalous Hall effect (AHE) in a hexagonal ferromagnetic Fe₅Sn₃ single crystal with current along the b axis and a magnetic field normal to the bc plane. The intrinsic contribution of the anomalous Hall conductance σ_{AH}^{int} was approximately $613 \Omega^{-1} \text{ cm}^{-1}$, which was more than 3 times the maximum value in the frustrated kagome magnet Fe₃Sn₂ and nearly independent of the temperature over a wide range between 5 and 350 K. The analysis results revealed that the large AHE was dominated by a common, intrinsic term, while the extrinsic contribution, i.e., the skew scattering and side jump, turned out to be small. In addition to the large AHE, it was found the types of majority carriers changed at approximately 275 and 30 K, consistent with the critical temperatures of the spin reorientation. These findings suggest that the hexagonal ferromagnetic Fe₅Sn₃ single crystal is an excellent candidate to use for the study of the topological features in ferromagnets.

*Authors to whom correspondence should be addressed. Email: wenhong.wang@iphy.ac.cn

I. INTRODUCTION

The anomalous Hall effect (AHE), discovered by E. H. Hall a century ago [1], has attracted generous interest from both the physics and materials communities because of its controversial physical origin [2-5] and wide practical application [6]. In contrast to the electromagnetic origin of the ordinary Hall effect, $\rho_{yx}^{OH} = R_0 \mu_0 H$, the AHE contribution to the total Hall resistivity, $\rho_{yx} = \rho_{yx}^{OH} + \rho_{yx}^{AH}$, is determined solely by the spontaneous magnetization, $\rho_{yx}^{AH} = R_s M$ [7-9]. In the formula, R_0 and R_s are the ordinary and anomalous Hall coefficients, respectively. The magnetization M is a function of the external field H . On the theoretical side, Karplus and Luttinger (K-L) proposed the intrinsic mechanism that considered the ρ_{yx}^{AH} was quadratic in the longitudinal zero-field resistivity ρ_{xx} ($\rho_{yx}^{AH} \propto \rho_{xx}^2$) [2]. The K-L mechanism is understood as the effect of the spin-orbit interaction of polarized conduction electrons at an external electrical field. With this in mind, Smit [3,4] and Berger [5] identified two basic extrinsic mechanisms, skew-scattering and side-jump, which were linear ($\rho_{yx}^{AH} \propto \rho_{xx}$) and quadratic ($\rho_{yx}^{AH} \propto \rho_{xx}^2$) for ρ_{xx} , respectively. These mechanisms are commonly understood to be a result of asymmetric scattering from the spin-orbit interaction acting on conducting electrons or impurities. Recently, the intrinsic mechanism (K-L) has been considered to be linked to the Berry curvature of electronic band structure in momentum space, which induces an anomalous velocity perpendicular to the electric field [10,11].

On the experimental side, a few materials with complex magnetic structures have been found to have non-trivial band structures, such as the non-collinear antiferromagnet Mn_3Sn [12,13], frustrated kagome ferromagnet Fe_3Sn_2 [14,15], ferromagnetic Weyl semimetal $\text{Co}_3\text{Sn}_2\text{S}_2$ [16-18], and two-dimensional ferromagnet Fe_3GeTe_2 [19]. The non-trivial band structure always couples with a large Berry curvature [20] that acts like a fictitious magnetic field and generates a large intrinsic AHE [10,11]. Therefore, to some extent, a large AHE has become a symbol of searching

for topological materials. The intrinsic magnetic topological materials are the ideal candidates with which to explore the relationship between magnetism and topological band structures, which has propelled researchers to find more intrinsic magnetic topological materials.

In this paper, a large AHE in a hexagonal ferromagnetic Fe_5Sn_3 single crystal, which was mostly induced by the intrinsic mechanism, is reported. As shown in Figs. 1(a) and 1(b), Fe_5Sn_3 single crystals crystallized in a hexagonal crystal structure with the space group $P6_3/mmc$ ($a=b=4.224 \text{ \AA}$, $c=5.222 \text{ \AA}$). The Fe and Fe-Sn layers were arranged alternately along the c axis. Two different sites for the Fe atoms were located at Fe-I (0, 0, 0) and Fe-II ($1/3, 2/3, 1/4$) and the occupancies of the Fe-I and Fe-II are 1 and 0.67, respectively. Furthermore, the Fe-II sites always formed vacancies or disorder that were related to the synthesis temperatures and they further affected the Curie temperature T_C and the saturation magnetization M_s of the Fe_5Sn_3 [21,22]. The easy magnetization axis of the Fe_5Sn_3 tended to be the b axis [23]. However, the detailed magnetic structure of Fe_5Sn_3 awaits further study.

II. EXPERIMENTAL DETAILS

Single crystals of Fe_5Sn_3 were synthesized by the Sn-flux method with a molar ratio of Fe:Sn = 1:17. Fe (purity 99.95%) and Sn (purity 99.99%) grains were mixed and placed in an alumina crucible. The crucible was then sealed in a tantalum tube under a partial Argon atmosphere. Finally, the tantalum tube was sealed in a quartz tube to avoid oxidation. The quartz tube was placed in a furnace and kept at $1150 \text{ }^\circ\text{C}$ for two days to obtain a homogeneous metallic solution, and then the quartz tube was cooled from $910 \text{ }^\circ\text{C}$ to $800 \text{ }^\circ\text{C}$ at a rate of $1.5 \text{ }^\circ\text{C/h}$ and kept at $800 \text{ }^\circ\text{C}$ for two days to reduce the defects in the single crystals. To obtain isolated single crystals, the quartz tube was moved quickly into the centrifuge to separate the excess Sn flux at $800 \text{ }^\circ\text{C}$. As shown in the inset of Fig. 1(c), the free-growing single crystal of Fe_5Sn_3 appeared as a bar (approximately 2–5 mm long) with a hexagonal section. X-ray diffraction (Fig. 1(c)) and high-resolution morphology (Fig. 1(d)) examinations were conducted at room temperature with a Bruker D2 X-ray machine with Cu K_α radiation ($\lambda=1.5418 \text{ \AA}$) and

a scanning transmission electron microscope (JEOL ARM200F), respectively. To confirm the orientations of the single crystal planes, the single crystal X-ray diffraction (see Fig. S1 of the Supplementary Material [24]) was also measured. These results strongly suggested that the rectangular plane was the bc plane and the long side was the c axis. Energy dispersive X-ray spectroscopy (EDS) measurements showed that the average ratio of iron in the samples was approximately 61.67% (see Table S1 and Fig. S2 [24]), which was less than the standard stoichiometric ratio. The magnetization and electrical transport were measured in a Quantum Design MPMS-XL and PPMS-9, respectively. To measure the electrical transport, the single crystals were cut into a rectangle with dimensions of 1.5×0.5×0.1 mm and a standard four-probe method was applied. To eliminate the influence of the voltage probe misalignment, the longitudinal (ρ_{xx}) and transverse (ρ_{yx}) resistivities were measured for both positive and negative fields ($\rho_{xx}(\mu_0 H) = (\rho_{xx}(+\mu_0 H) + \rho_{xx}(-\mu_0 H))/2$ and $\rho_{yx}(\mu_0 H) = (\rho_{yx}(+\mu_0 H) - \rho_{yx}(-\mu_0 H))/2$).

III. RESULTS AND DISCUSSION

Figure 2(a) shows the zero field cooling curves (ZFC) at 0.5 T with the magnetic fields H parallel to the b and c axis. It is clearly shown in the figure that the easy magnetization axis of the single crystal tended to be the b axis and the Curie temperature T_C was approximately 600 K, consistent with early reports [22,23]. The inset of Fig. 2(a) shows the low temperature details of the magnetization with H along the c axis at 0.5 T. Two obvious kink points appeared at approximately 50 and 125 K (the more detailed M-T curves with H along the c axis are shown in Fig. S3 [24]). The uniaxial magnetic anisotropy coefficient $K_u = \mu_0 M_s H_k / 2$ decreased with increasing temperature, shown in Fig. 2(b), suggesting that the easy axis gradually rotated from the ab plane to the c axis with increasing temperature. The H_k term in the formula is the anisotropy effective field that is defined as the critical field above the difference in magnetization between the two magnetic field directions ($H//b$ axis and $H//c$ axis) becoming smaller than 2%. Remarkably, there were also two clear kink points at 250 and 125 K. However, the curves of the heat capacity C_p (10–100 K) and the differential

scanning calorimetry (DSC, 100–400 K), shown in Fig. S5 [24], did not exhibit any obvious peaks for the heating and cooling processes. Therefore, these kink points of the M-T and K_u -T curves near 50, 125, and 250 K could all be induced by the continuous rotation of the easy axis from the ab plane to the c axis with increasing temperature rather than the crystallographic phase transition. However, a full accounting of the magnetic structure awaits further analysis. The inset of Fig. 2(b) shows the magnetization curves with H along the b axis and c axis at 300 K (more detailed M-H curves are shown in Fig. S4 [24]). It is clearly shown in the figure that the saturation fields along the two axes were approximately 0.2 T (b axis) and 1.5 T (c axis).

The temperature dependence of the longitudinal resistivity ρ_{xx} along the b axis for zero field and 5 T are shown in Fig. 2(c). The curves of ρ_{xx} exhibited typical metallic behavior at the zero field and at 5 T. There was a clear slope change of the zero field ρ_{xx} curve near 50 K and it was conspicuously suppressed at 5 T, which also implied that the kink points of M-T and K_u -T curves near 50 K were induced by the magnetic structure transition. The inset shows the curves of $d\rho_{xx}/dT$ at zero field. The slopes of ρ_{xx} appeared to have an obvious change below 125 K and the slopes reached a maximum at approximately 30 K, which was consistent with the changes of magnetization near these temperatures. The magnetoresistance ($MR = (\rho_{xx}(\mu_0 H) - \rho_{xx}(0)) \times 100\% / \rho_{xx}(0)$) is shown in Fig. 2(d). It is clearly shown in the figure that the sign of the MR was opposite at low and high temperatures and the turning point was approximately 50 K (more detailed MR curves are shown in Fig. S6(c) [24]). The negative MR was obviously induced by spin-dependent scattering in the magnetic systems [25] and the positive MR may relate to the complex magnetic structure [26] at the low-temperature zone in Fe_5Sn_3 . The sign change was obviously associated with the transformation of the magnetic structure with temperature, which was similar to the situation in Fe_3Sn_2 [27].

Figure 3(a) shows the magnetization curves M-H with H normal to the bc plane at various temperatures. The M-H curves displayed typical soft ferromagnet behavior with a coercive field that was almost zero and a saturation field of approximately 1 T, which was between the values at H along the b axis and c axis. The saturation magnetization

was approximately $2.29\mu_B/\text{Fe}$ at 5 K, which was slightly larger than the saturation magnetization in early reports [21,23,28]. The discrepancy arose from the different vacancies or the disorder of Fe-II atoms in the samples that were synthesized at different temperatures [22]. The data for the Hall resistivity ρ_{yx} with the current along the b axis and H normal to the bc plane are shown in Fig. 3(b). The magnetic field dependence curves of ρ_{yx} appeared to have a typical AHE for the Fe_5Sn_3 , and more than one sample was measured. The more detailed magnetization and electrical transport data are shown in Figs. S4, S6, and S7 [24].

To further study the AHE of Fe_5Sn_3 , a detailed analysis was made, the results of which is shown in Figs. 4(a)–4(d). Above the saturation field (approximately 1 T), the M was replaced by the saturation magnetization M_s and the anomalous hall resistivity ρ_{yx}^{AH} became a constant. With a linear fit of the ρ_{yx} at the high-field region (above 2 T), which is shown by the red dashed line in Fig. 3(b), the slopes and intercepts corresponded to R_0 and the anomalous Hall resistivity $\rho_{yx}^{AH} = R_s M_s$. The values of M_s were taken from the magnetization curves at 5 T. The curve of R_0 -T is shown in Fig. 4(a). The signs of R_0 represent the types of majority carriers. An interesting phenomenon was that the signs of R_0 exhibited obvious changes at approximately 275 and 30 K in Fe_5Sn_3 . The signs of R_0 were positive when the temperature was above 275 K or below 30 K, which meant that the majority carriers were electrons. The majority carriers changed into holes between 30 and 275 K. The inset of Fig. 4(a) shows the carrier concentrations ($n=1/|e|R_0$), which also appeared to have two local maximum points at 275 and 30 K. R_0 did not change its sign near 125 K, but the R_0 values appeared to have a local extreme value. The transformation temperatures showed a small discrepancy for different samples (see Fig. S7(c) [24]), which was because of the slight difference of the vacancies or the disorder in the site of Fe-II [22]. The facts described above are reminders of the continuous rotation of the easy axis, as shown in Figs. 2(a) and 2(b), which was also similar to the situations of the 2H metallic transition-metal dichalcogenides [29-31] and the film of the metallic oxides CaRuO_3 and SrRuO_3 [32]. The unconventional relationship between R_0 and T may have been caused by a tight

correlation between the magnetic structure and the Fermi surface in Fe₅Sn₃. Figure 4(b) shows the temperature dependence of R_s , which increases monotonically with temperature. The inset shows the scaling coefficient $S_H = R_s/\rho_{xx}^2$, which was a material-specific scale factor [33,34].

To help understand the origin of the AHE in the Fe₅Sn₃, the function dependencies of $\log\rho_{yx}^{AH}$ and $\log\rho_{xx}$ are shown in Fig. 4(c). The slope of the linear fitting α was equal to 2.06, which meant that the AHE of Fe₅Sn₃ could be from the K-L mechanism [2] or the side jump mechanism [5], because both showed the same quadratic relationship between ρ_{yx}^{AH} and ρ_{xx} [35]. To further ascertain the mechanism of the AHE, a recently discovered method [36–38] was used to separate the intrinsic and extrinsic contributions, as shown in Fig. 4(d). The inset of Fig. 4(d) shows the scaling behavior of ρ_{yx}^{AH} versus $\rho_{xx}(0\text{ K})$. The red curve in the figure represents the fitting equation $\rho_{yx}^{AH} = \alpha\rho_{xx0} + \beta\rho_{xx0}^2 + \gamma\rho_{xx}^2$, where ρ_{xx0} is the residual resistivity (the value of ρ_{xx} at 2 K was used), and α , β , and γ are the coefficients of the skew scattering, side-jump, and intrinsic terms, respectively. As shown in Fig. 4(d), a large intrinsic value ($\sigma_{AH}^{int} \sim 613\text{ }\Omega^{-1}\text{ cm}^{-1}$) was obtained for the anomalous Hall conductance (AHC) in Fe₅Sn₃, which was more than 3 times the maximum value in Fe₃Sn₂ ($\sigma_{AH}^{int} \sim 200\text{ }\Omega^{-1}\text{ cm}^{-1}$) [14]. The value of the AHC calculated with density functional theory (DFT) using the Vienna ab-initio simulation package (VASP) [40] and WannierTools [41] package was approximately $507.7\text{ }\Omega^{-1}\text{ cm}^{-1}$, which was close to the experimental value and which further demonstrated that the large AHC was mostly induced by the intrinsic mechanism. Moreover, the large AHC was robustly independent in a wide range of temperatures between 5 and 350 K despite the complex magnetic structure transformation, which indicates that the Berry curvature of the momentum space was very stable. For comparison, the typical physical parameters of Fe₅Sn₃ and Fe₃Sn₂ are summarized as shown in Table I. As a result, it was found that the K_u and M_s values of Fe₅Sn₃ were also larger than those of Fe₃Sn₂, so they could be a good pair of samples with which to study the correlation between the topological and magnetic properties.

IV CONCLUSIONS

In summary, a detailed investigation of the magnetic and electrical transport properties of hexagonal ferromagnetic Fe₅Sn₃ single crystals is presented in this paper. The MR signs changed at 50 K and the types of majority carriers changed at approximately 275 and 30 K, which was tightly related to the magnetic structure transformation. Moreover, the AHC in Fe₅Sn₃ was mostly induced by the intrinsic mechanism and the value of σ_{AH}^{int} was approximately 613 $\Omega^{-1} \text{ cm}^{-1}$, which was more than three times the maximum value in the frustrated kagome magnet Fe₃Sn₂ single crystals. More importantly, the large intrinsic AHC turned out to be almost independent of temperatures, indicating that the hexagonal ferromagnetic Fe₅Sn₃ single crystal was an excellent candidate for studying the topological features in ferromagnets.

ACKNOWLEDGEMENTS

This work is supported by the National Key R&D Program of China (Grant Nos. 2017YFA0206303), National Natural Science Foundation of China (Nos. 11974406 and 11874410).

References

- [1] E. Hall, *Philos. Mag* **12**, 157 (1881).
- [2] R. Karplus and J. M. Luttinger, *Phys. Rev.* **95**, 1154 (1954).
- [3] J. Smit, *Physica* **21**, 877 (1955).
- [4] J. Smit, *Physica* **24**, 39 (1958).
- [5] L. Berger, *Phys. Rev. B* **2**, 4559 (1970).
- [6] J. Moritz, B. Rodmacq, S. Auffret, and B. Dieny, *J. Phys. D: Appl. Phys.* **41**, 135001 (2008).
- [7] A. Kundt, *Wied. Ann* **49**, 257 (1893).
- [8] E. M. Pugh, *Phys. Rev.* **36**, 1503 (1930).
- [9] E. M. Pugh and T. W. Lippert, *Phys. Rev.* **42**, 709 (1932).
- [10] T. Jungwirth, Q. Niu, and A. H. MacDonald, *Phys. Rev. Lett.* **88**, 207208 (2002).
- [11] M. Onoda and N. Nagaosa, *J. Phys. Soc. Jpn.* **71**, 19 (2002).
- [12] S. Nakatsuji, N. Kiyohara, and T. Higo, *Nature* **527**, 212 (2015).
- [13] K. Kuroda, T. Tomita, M.T. Suzuki, C. Bareille, A. A. Nugroho, P. Goswami, M. Ochi, M. Ikhlas, M. Nakayama, S. Akebi, R. Noguchi, R. Ishii, N. Inami, K. Ono, H. Kumigashira, A. Varykhalov, T. Muro, T. Koretsune, R. Arita, S. Shin, Takeshi Kondo and S. Nakatsuji., *Nat. Mater.* **16**, 1090 (2017).
- [14] L. Ye, M. Kang, J. Liu, F. von Cube, C. R. Wicker, T. Suzuki, C. Jozwiak, A. Bostwick, E. Rotenberg, D. C. Bell, L. Fu, R. Comin, and J. G. Checkelsky, *Nature* **555**, 638 (2018).

- [15] J. X. Yin, S. S. Zhang, H. Li, K. Jiang, G. Chang, B. Zhang, B. Lian, C. Xiang, I. Belopolski, H. Zheng, T. A. Cochran, S.Y. Xu, G. Bian, K. Liu, T.R. Chang, H. Lin, Z.Y. Lu, Z. Wang, S. Jia, W.Wang and M. Z. Hasan, [Nature](#) **562**, 91 (2018).
- [16] E. Liu, Y. Sun, N. Kumar, L. Muechler, A. Sun, L. Jiao, S. Y. Yang, D. Liu, A. Liang, Q. Xu, J. Kroder, V. Süß, H. Borrmann, C. Shekhar, Z. Wang, C. Xi, W. Wang, W. Schnelle, S. Wirth, Y. Chen, S. T. B. Goennenwein, and C. Felser, [Nat. Phys.](#) **14**, 1125 (2018).
- [17] D. F. Liu, A. J. Liang, E. K. Liu, Q.N.Xu,Y. W. Li, C. Chen, D. Pei, W. J. Shi, S. K. Mo, P. Dudin, T. Kim, C. Cacho,G. Li, Y. Sun, L. X. Yang, Z. K. Liu, S. S. P. Parkin, C. Felser, and Y. L. Chen , [Science](#) **365**, 1282 (2019).
- [18] N. Morali, R. Batabyal, P. K. Nag, E. Liu, Q. Xu, Y. Sun, B. Yan, C. Felser, N. Avraham, and H. Beidenkopf , [Science](#) **365**, 1286 (2019).
- [19] K. Kim, J. Seo, E. Lee, K. T. Ko, B. S. Kim, B. G. Jang, J. M. Ok, J. Lee, Y. J. Io, W. Kang, J. H. Shim, H. W. Yeom, B. II Min, B. J. Yang, and J. S. Kim, [Nat. Mater.](#) **17**, 794 (2018).
- [20] D. Xiao, M.-C. Chang, and Q. Niu, [Rev. Mod. Phys.](#) **82**, 1959 (2010).
- [21] H. Yamamoto, [J. Phys. Soc. Jpn.](#) **21**, 1058 (1966).
- [22] G. Trumphy, E. Both, C. Djéga-Mariadassou, and P. Lecocq, [Phys. Rev. B](#) **2**, 3477 (1970).
- [23] B. C. Sales, B. Sagarov, M. A. McGuire, D. J. Singh, and D. S. Parker, [Sci Rep](#) **4**, 7024 (2014).
- [24] See Supplemental Material for details of single crystal X-ray diffraction measurement, the energy dispersive X-ray spectroscopy (EDS), magnetization curves with H parallel to b axis and c axis, The heat capacity C_p and differential scanning calorimetry (DSC) curves, the detailed magnetization and Hall resistivity's data sample 1 (S1) with current parallel to b axis and H normal to bc plane of at various temperature, and the electrical transport measurement of sample 2 (S2).
- [25] B. Raquet, M. Viret, E. Sondergard, O. Cespedes, and R. Mamy, [Phys. Rev. B](#) **66**, 024433 (2002).
- [26] S. Gupta, K. G. Suresh, and A. K. Nigam, [J. Alloy. Compd.](#) **586**, 600 (2014).
- [27] H. Li, B. Ding, J. Chen, Z. Li, Z. Hou, E. Liu, H. Zhang, X. Xi, G. Wu, and W. Wang, [Appl. Phys. Lett.](#) **114**, 192408 (2019).
- [28] A. Dianoux, B. Malaman, and T. Mazet, [Solid State Commun.](#) **260**, 40 (2017).
- [29] H. N. S. Lee, M. Garcia, H. McKinzie, and A. Wold, [J. Solid State Chem.](#) **1**, 190 (1970).
- [30] M. Naito and S. Tanaka, [J. Phys. Soc. Jpn.](#) **51**, 219 (1982).
- [31] S. V. Borisenko, A. A. Kordyuk, A. N. Yaresko, V. B. Zabolotnyy, D. S. Inosov, R. Schuster, B. Büchner, R. Weber, R. Follath, L. Patthey, and H. Berger, [Phys. Rev. Lett.](#) **100**, 196402 (2008).
- [32] S. C. Gausepohl, M. Lee, R. A. Rao, and C. B. Eom, [Phys. Rev. B](#) **54**, 8996 (1996).
- [33] M. Lee, Y. Onose, Y. Tokura, and N. P. Ong, [Phys. Rev. B](#) **75**, 192403 (2007).
- [34] S. Friedemann, M. Brando, W. J. Duncan, A. Neubauer, C. Pfleiderer, and F. M. Grosche, [Phys. Rev. B](#) **87**, 024410 (2013).
- [35] N. Nagaosa, J. Sinova, S. Onoda, A. H. MacDonald, and N. P. Ong, [Rev. Mod. Phys.](#) **82**, 1539 (2010).
- [36] Y. Tian, L. Ye, and X. Jin, [Phys. Rev. Lett.](#) **103**, 087206 (2009).
- [37] D. Hou, G. Su, Y. Tian, X. Jin, S. A. Yang, and Q. Niu, [Phys. Rev. Lett.](#) **114**, 217203 (2015).
- [38] L. Wu, K. Zhu, D. Yue, Y. Tian, and X. Jin, [Phys. Rev. B](#) **93**, 214418 (2016).
- [39] Z. Hou, W. Ren, B. Ding, G. Xu, Y. Wang, B. Yang, Q. Zhang, Y. Zhang, E. Liu, F. Xu, W. Wang, G. Wu, X. Zhang, B. Shen, and Z. Zhang, [Adv. Mater.](#) **29**, 1701144 (2017).
- [40] G.Kresse, and J. Furthmüller, [Phys. Rev. B](#) **54**, 11169 (1996).
- [41] Q. Wu, S. Zhang, H.-F. Song, M. Troyer, and A. A. Soluyanov, [Comput. Phys. Commun.](#) **224**, 405–416 (2018).

Figure caption

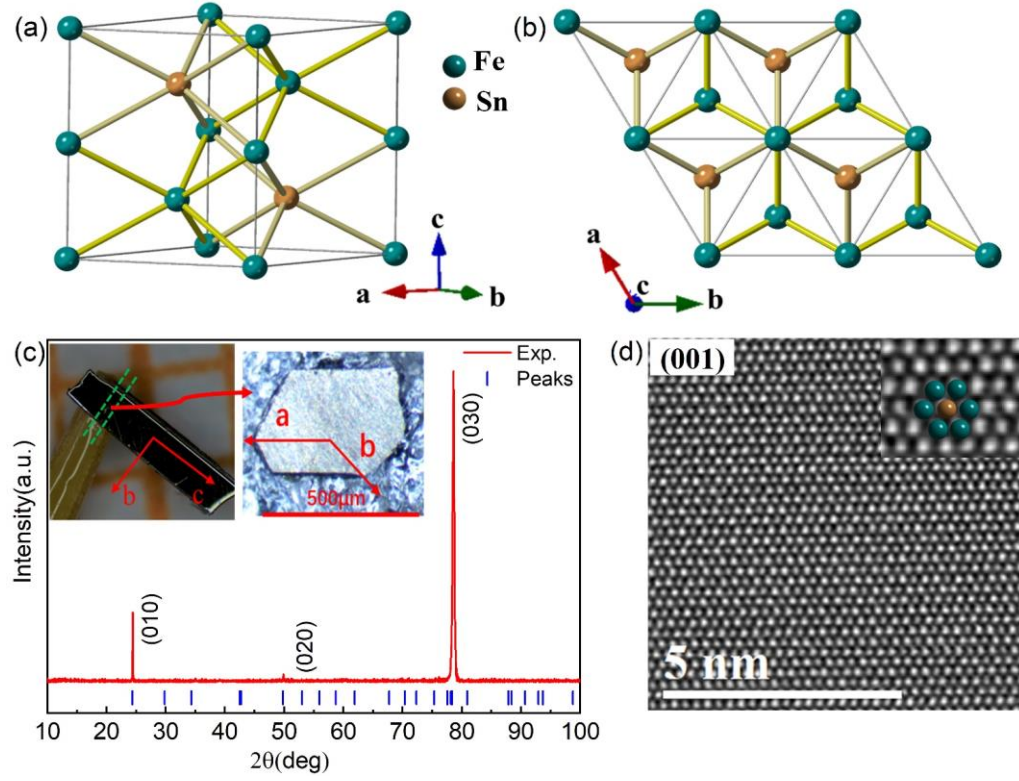


FIG. 1. (a) Side and (b) top views of Fe_5Sn_3 crystal structure. (c) X-ray diffraction pattern of bc plane. Inset contains the photographs of a single crystal (left) and its cross-section (right) cut along the green dashed line. (d) High-resolution scanning transmission electron microscopy image of (001) plane.

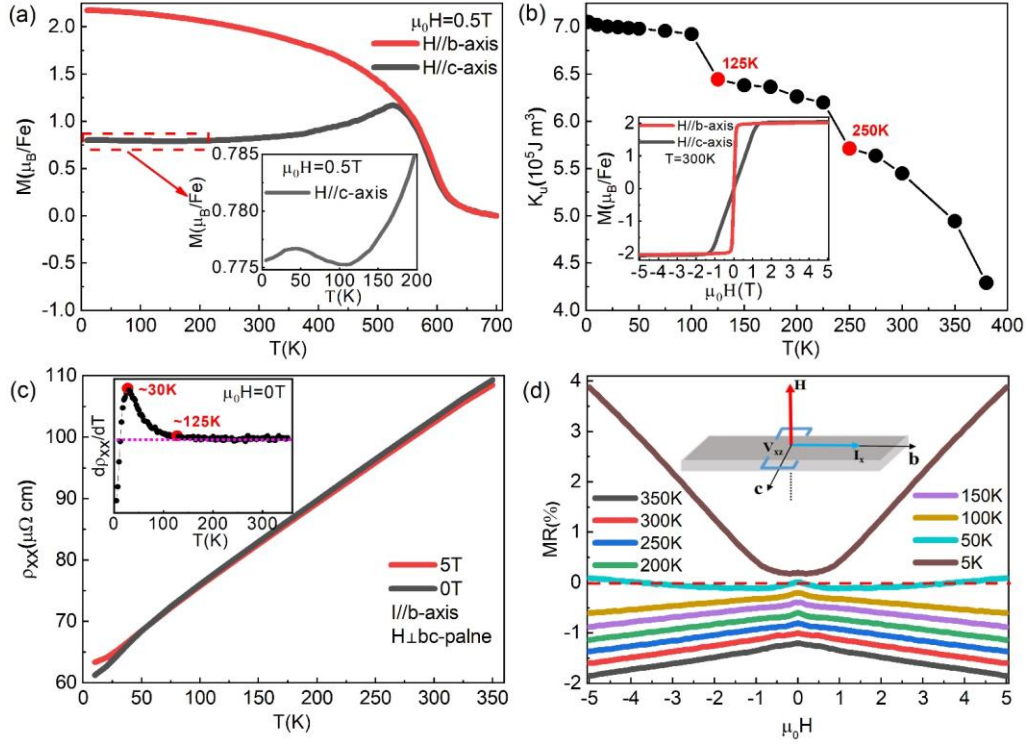


FIG. 2. (a) Zero field cooling (ZFC) curves at 0.5 T along b axis and c axis. Few differences existed between the zero field cooling and field cooling (FC) curves at 0.5 T. To clearly show the M-T curves, only the ZFC curves are shown. Inset shows the low temperature details of the curve with H along the c axis. (b) Temperature dependence of the uniaxial magnetic anisotropy coefficient K_u . Inset shows the magnetization curves along the b axis and c axis at 300 K. (c) Resistivity along the b axis for zero field and 5 T. Inset shows the curve of $d\rho_{xx}/dT$ for zero field. (d) Magnetic field dependence of magnetoresistance obtained in the temperature range 5–350 K, with the magnetic fields applied normal to the bc plane and the current along b axis. Red dashed line represents the zero of MR. Inset shows directions of the current and magnetic field in the measurements.

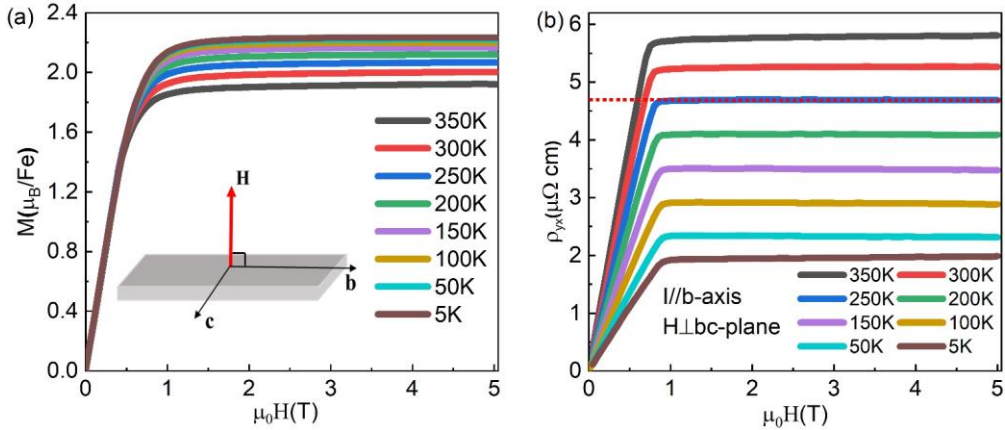


FIG. 3. (a) Magnetization curves at H normal to bc plane. Inset shows the schematic of the magnetic measurement. (b) Hall resistivity ρ_{yx} at current along the b axis and H normal to the bc plane. Red dashed line represents the linear fit of ρ_{yx} at the high field region at 250 K. For clarity, only some data for the temperature are shown. More detailed data are shown in Figs. S3(a) and S3(b) in the Supplementary Material [24].

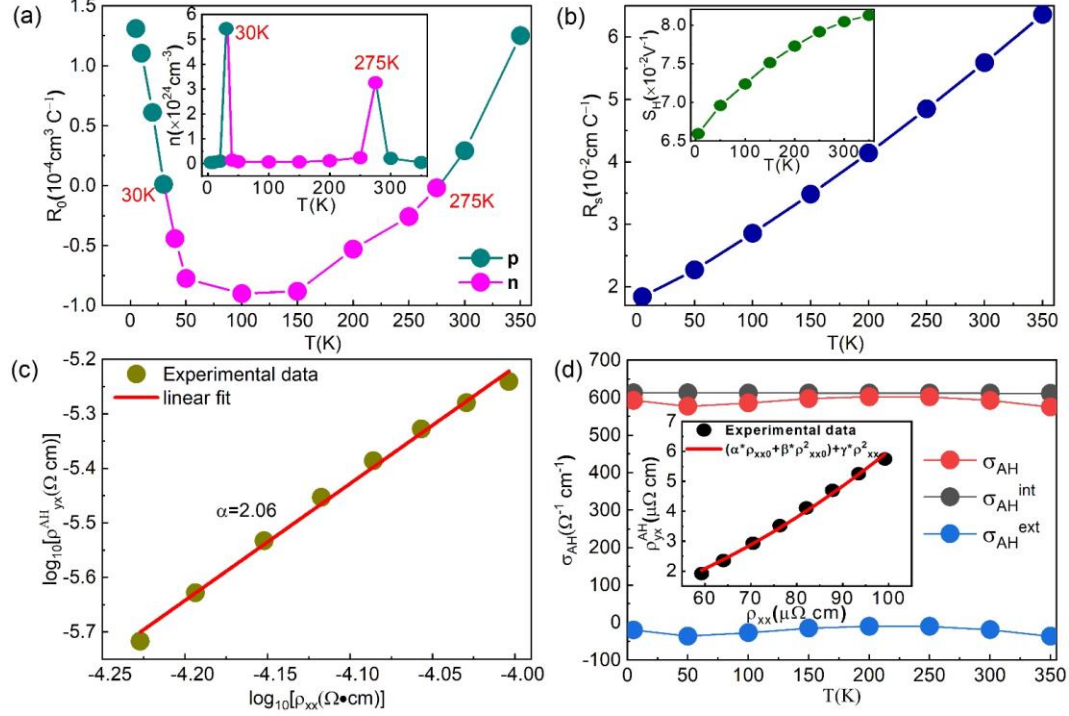


FIG.4. Temperature dependence of (a) ordinary Hall coefficient R_0 and (b) anomalous Hall coefficient R_s . Inset of (a) shows the current concentration and inset of (b) shows the scaling coefficient S_H . (c) Scaling behavior of $\log \rho_{yx}^{AH}$ vs $\log \rho_{xx}$. Red line is the linear fit. (d) Temperature dependence of the anomalous Hall conductance. Inset shows the plot of ρ_{yx}^{AH} vs. ρ_{xx} .

Table

TABLE I. Experimental and calculated values of intrinsic anomalous Hall conductance $\sigma_{AH}^{\text{int-exp}}$ and $\sigma_{AH}^{\text{int-cal}}$ uniaxial magnetic anisotropy coefficient K_u , saturation magnetization M_s and Curie temperature T_C of Fe_3Sn_2 [14,39] and Fe_5Sn_3 .

	$\sigma_{AH}^{\text{int-exp}}$ ($\Omega^{-1} \cdot \text{cm}^{-1}$)	$\sigma_{AH}^{\text{int-cal}}$ ($\Omega^{-1} \cdot \text{cm}^{-1}$)	K_u ($\times 10^5 \text{ J/m}^3$)	M_s (μ_B/Fe)	T_C (K)
Fe_5Sn_3	~613	~507.7	5.45 (300 K)	~2.29 (5 K)	600
Fe_3Sn_2	~200	—	3.04 (300 K)	~1.97 (5 K)	640